Processing parameters in laser powder bed fusion metal additive manufacturing

J.P. Oliveira [a,b], A.D. LaLonde [d], J. Ma [c,*]

[a] UNIDEMI, Department of Mechanical and Industrial Engineering, NOVA School of Science and Technology, Universidade NOVA de Lisboa, 2829-516 Caparica, Portugal
[b] CENIMAT/I3N, Department of Materials Science, NOVA School of Science and Technology, Universidade NOVA de Lisboa, 2829-516 Caparica, Portugal
[c] Department of Materials Science and Engineering, University of Virginia, 395 McCormick Road, Charlottesville, VA 22904, United States
[d] Booz Allen Hamilton, 8283 Greensboro Drive, McLean, VA 22102, United States

HIGHLIGHTS

- Comparison between laser welding and laser-based additive manufacturing parameters is established.
- Major process parameters during laser-based additive manufacturing and their influence are discussed.
- Remedies for avoid several problems found during additive manufacturing are proposed.

GRAPHICAL ABSTRACT
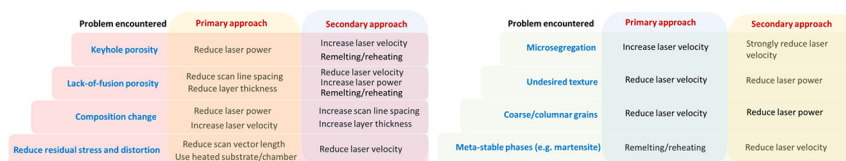
ARTICLE INFO

ABSTRACT

As metallic additive manufacturing grew in sophistication, users have requested greater control over the systems, namely the ability to fully change the process parameters. The goal of this manuscript is to review the effects of major process parameters on build quality (porosity, residual stress, and composition changes) and materials properties (microstructure and microsegregation), and to serve as a guide on how these parameters may be modified to achieve specific design goals for a given part. The focus of this paper is on laser powder bed fusion, but elements can be applied to electron beam powder bed fusion or direct energy deposition techniques.

1. Introduction

Metal-based additive manufacturing (AM) enables manufacturing of metal parts with a high degree of geometric complexity and promises to significantly reduce cost, time, and energy consumption of production [1]. Furthermore, AM allows for parts nearing the end of lifetime to be repaired or refurbished, obsolete parts to be replaced, and enables fabrication in remote locations [2]. Not surprisingly, intense interest in AM technologies has built up within the defense, energy, aerospace, and biomedical industries among others. In particular, laser-based powder bed fusion (L-PBF) technology has emerged as a leading candidate for fabrication of mission-critical components.

Because of the complexity of the laser powder bed fusion process, the original equipment manufacturers of metal AM systems have developed sets of optimized processing conditions for each material. These include both machine settings which are not generally changed, and process parameters which can be modified from build to build. In modern laser powder bed fusion systems, there are over 100 of such processing parameters, most commonly-considered among which include laser power, layer thickness, laser scan velocity, distance between successive laser passes (also known as hatch distance) and scanning strategies (laser scanning pattern on each layer) – see Fig. 1. The optimized parameters are empirically derived to generally produce dense materials,

* Corresponding author.
  E-mail address: jm@virginia.edu (J. Ma).

minimize defects, reduce surface roughness, increase build rate, and produce parts with acceptable material properties. To date, parameters provided by machine manufacturers are typically developed to provide the best result in the material produced as a compromise of these competing (and interdependent) priorities. As there are infinite possibilities for part design, it is not possible to have one parameter set that will be fully optimized for all part features (thin walls, thick sections, overhangs, or others), material performance and process productivity. As a result, general parameter sets are developed to meet as many priorities and build geometries as possible. However, significant opportunities remain for further optimization of specific parts, geometries and applications. Additionally, optimized parameters continuously change even for the same material as manufacturers release new machine models and technology and processes are further developed. Historically, AM systems have been offered as a black-box turn-key solution where customers print parts at the recommended settings and are advised to change little to nothing.

As AM processes become better understood and the field gradually grew in sophistication, users have requested greater control over the systems. Among other things, this includes the ability to change the process parameters, as well as to customize powder stock which may include non-standard materials. As a result, some manufacturers now offer "open system" options, where customization and modifications are possible to optimize the build process for specific needs. One may wonder what could be gained by modifying the processing parameters over sets recommended by the manufacturer. At the same time, those wishing to print with new materials often encounter difficulty in finding appropriate parameters since optimized sets are not available. An excellent review by DebRoy et al. [1] is available and details the mechanisms of most build-related issues (porosity, residual stress, preferential evaporation, among others) and grain morphology and texture developed during the L-PBF process. Thus, the goal of this paper is complement existing surveys by: i) more directly address how major L-PBF process parameters can be manipulated to change build-related and materials-related aspects of a part, and when it may be appropriate to utilize non-optimized parameters to achieve specific goals, ii) update on more recent development in the field, and iii) focus on certain materials-related topics that were not discussed in detail previously such as microsegregation. The focus of this paper is directed for laser powder bed fusion, but elements can be applied to electron beam powder bed fusion or direct energy deposition techniques. While specific alloy systems are referenced in specific sections, the discussion in this work is materials-agnostic and can be broadly applicable.
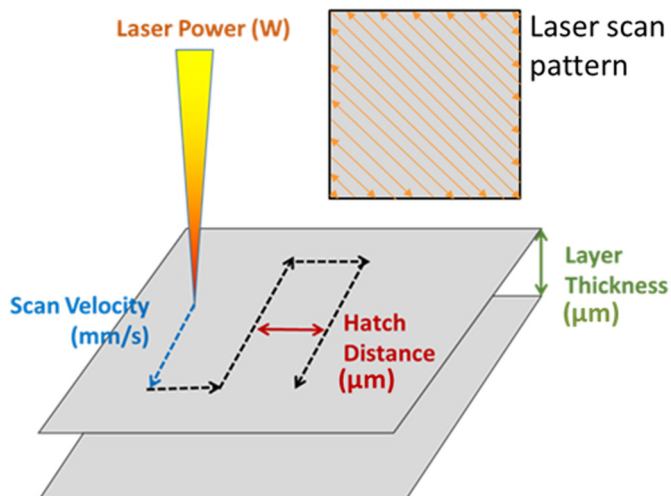

Fig. 1. Common process parameters in laser powder bed fusion AM.

2. Background

2.1. Laser welding

The laser additive manufacturing process shares many commonalities with the well-established laser welding and cutting/ablation techniques [3]. The ability to have high power lasers capable to focus the laser energy into very small spots results in a very high-density energy process. The most used lasers in the area of materials processing, which include cutting, surface treatments and welding, are CO_2 lasers [3,4], Nd:YAG lasers [5,6] and fiber lasers [7,8]. Due to the stimulated emission of radiation, all photons will have the same wavelength, will be in phase in both space and time, and will travel in the same direction. As such, one can state that laser radiation has the following three main characteristics: monochromaticity, coherency and directionally low divergence in both space and time. The last two characteristics allow good focus of the radiation which is of great importance for several advanced manufacturing processes based on laser radiation.

When the laser energy hits the material, the photons will be absorbed and converted into heat that will dissipate through conduction. Melting can only occur if the energy that is introduced into the material is higher than the dissipated energy. Several process parameters will influence the melted and solidified material and interface with the surrounding material. Influential variables can be related to the laser itself, such as wavelength, output power, operation mode and beam quality, or to the manipulation systems and materials, such as the optical and physical properties of the material as a function of temperature. The laser can be operated in either pulse or continuous modes. In the former, the pulse shape, frequency and duration, and the peak energy are most important operation parameters to control [9,10], whereas in the latter the laser power and welding speed must be controlled [11,12]. Additionally, shielding gas is required to prevent oxidation and evaporation phenomena of the molten pool and heat affected zone [13,14]. Further benefits can be realized from the shielding gas as it will improve energy coupling between the laser and the material, blowing away the plasma that is formed above the surface.

In conventional laser welding, the presence of porosity is attributed to the weld pool dynamics. When there is turbulent flow of the weld pool pore formation is promoted, imperfect keyhole collapse can occur, and rejection of elements, such as hydrogen, from the solid phase during solidification may happen. This turbulent flow is driven by Marangoni flows [15,16], typical of high energy melting processes as those occurring during laser powder bed fusion. Incorporation of foreign elements can also contribute to porosity formation in the welded joints [17–20]. The presence of pores in welded structures is detrimental to their structural integrity, especially if the components are subjected to dynamic loading conditions.

For very high energy densities, typically on the order of 10^7 W/cm^2, the material can be vaporized, and the heat will be transmitted into the material in depth. A capillary of metallic vapor will form and is surrounded by the molten material that solidifies above the vapor, thus trapping the vapor within the material as a pore. This condition is known as the keyhole welding mode [21,22]. When the keyhole mode occurs, the weld is very narrow and typically has an aspect ratio (weld width/weld depth) significantly lower than 1. The shape and stability of the keyhole are determined by the forces that are being exerted on the molten pool. Gravity and surface tension will tend to close the capillary, whereas the beam pressure, vapor pressure and the recoil pressure will assist in maintaining it open.

If the energy density is lower, typically below 10^5 W/cm^2, the keyhole will not form, and in this case is referred to as conduction mode welding [23]. In a conduction mode weld the aspect ratio is larger than 1. During conduction mode welding the melt pool experiences strong stirring, resulting from the variations in surface tension and material density with temperature. In addition to keyhole and conduction modes there is a third mode that can occur, known as the mixed, or

transition welding mode, and is a combination of both conduction and keyhole welding modes. In the transition mode the energy density is between that of keyhole and conduction modes and the resulting weld pool typically has an aspect ratio near 1.

The formation of pores during laser welding is mainly controlled by two competing factors [16], the solidification rate and the backfilling speed of the molten pool. If the backfilling speed is not high enough to promote filling of the keyhole during solidification pores will be formed. As a result, controlling the solidification of the molten pool is key to avoid pore formation. Control over the solidification can be achieved by optimizing laser parameters so that the solidification process is delayed [24], thus allowing the liquid metal to fill the keyhole before solidification is complete. Another solution to prevent pore formation is through the use of electromagnetic fields to increase the filling speed of the keyhole during solidification [25]. Additionally, welding in vacuum was also seen to mitigate pore formation due to the lower pressure favoring the transport of evaporated metal towards the upper keyhole outlet [26]. However, the need of a vacuum system for laser welding may be detrimental for its implementation in industrial production owing to increased production costs.

Depending on the material that is being laser welded, the stability of the keyhole may or may not be a crucial factor for pore formation. For example, when laser welding aluminum alloys, the keyhole stability is crucial for pores formation [27]. On the other hand, for magnesium alloys the keyhole stability is not a major factor for pore formation [28]. The initial condition of the material that will be welded also influences pore formation: if small holes exist before welding, heating and reduction of the internal pressure during the process will favor their coalescence.

As previously stated, hydrogen can be responsible for pore formation during laser welding, especially in aluminum alloys [17]. One way to mitigate pore formation is through proper surface cleaning prior to welding [29]. Another possibility is to control the hydrogen content of the filler metal (if used), the purity of the shielding gas and ensuring that the shielding protection used during the process guarantees that entrapment of foreign elements into the molten pool is minimized or eliminated.

Another relevant laser parameter is the beam quality [30]. To assess the beam quality, or the energy distribution along the beam radius, one can use the beam parameter product (BPP) and/or the M^2 factor. The BPP is the product between the beam radius at the beam waist and the far-field beam divergence angle. The M^2 factor is defined by the ratio between the BPP and λ/π, where λ is the wavelength. For an ideal Gaussian beam the M^2 factor will have a value of 1. The beam quality, wavelength and beam diameter which exits the laser cavity will control the beam spot on the focus plane and the depth of focus. If the beam quality is poor, melting may not occur due to insufficient energy density.

The similarities between laser welding and laser-based additive manufacturing are significant. Therefore, the principles and knowledge of the laser welding technology and community are transferable and extremely valuable to the additive manufacturing field.

2.2. Laser-based additive manufacturing

The characteristics of AM-fabricated alloys often differ significantly from those obtained by conventional techniques such as casting. The most notable differences observed include: in the as-built condition, defects may be embedded in the part and high residual stress may be present due to the steep thermal gradients and non-uniform expansion/contraction experienced by the material [31,32]; in the microstructure, where unexpected phases can form due to the complex thermal history [33,34]; and composition, where the laser-material interaction and rapid solidification can also create both macro- and micro-scale differences in chemistry, with potential changes in the structural/functional properties of the parts [35,36]. Furthermore, the typically high cooling

rates in fusion-based AM techniques often result in a very small grain size in the produced parts, which can give raise to better mechanical properties when compared to other conventional manufacturing processes. Each of these differences resulting from the process often require post-processing to meet final application requirements and these additional steps will increase both the cost and the time required to produce parts [37,38].

Although the unique capabilities of metal-based AM are well recognized and the technologies continue to advance, significant gaps remain in order to bring AM technologies to full maturity. A major roadblock is the high degree of variability of materials properties in metal AM-fabricated parts, which poses serious challenges related to the qualification and certification (Q&C) of critical AM components. Another challenge is the requirement for post-processing in most AM-fabricated parts. Both challenges typically originate from two major sources: build effects and microstructure.

One of the possible reasons for the observed variability is the fact that a large portion of prior works on metal AM have focused only on a handful of major material systems, for example titanium [31,39–41] (mostly Ti-6Al-4V), nickel [32,37,42–45] (Inconel 625 and 718), and stainless steels [36,46,47] (304, 316/316L). Many of these material systems are not necessarily suitable for AM processing because of the process's complex and highly non-equilibrium nature. Consequently, materials become highly sensitive to variations in the processing conditions, which translates into a significant variability in observed properties.

It has been shown that the properties of some AM processed alloys are superior to their cast and wrought counterparts. The typically high cooling rates of fusion based AM processes can result in parts with very small grain size and, provided that manufacturing defects are kept to a minimum (or ideally non-existent), it is possible to expect that AM parts can possess improved mechanical properties in comparison with other more conventional manufacturing processes. AM technologies can be used as a platform for producing novel high-performance alloys for use in multiple industries and can also create graded structures (either microstructure or compositionally). In contrast, conventional processes are incapable of providing users such freedom to design their own materials.

Metallic AM techniques are based on rapid solidification. As the energy source is removed, cooling rates on the order of 10^5–10^6 K·s^{-1} can be reached [1]. In addition to the small grain size, rapid solidification can also lead to the formation of metastable phases and sometimes elemental partitioning as the melt is forced to solidify without adequate time for diffusion to reach equilibrium compositions. Besides these local microscopic changes in composition, the high temperatures reached during laser or electron beam melting can cause macroscopic changes in composition through differential evaporation [48]. These compositional changes may have dramatic effects on the properties of alloy systems that are extremely sensitive to composition. Finally, these two problems are exacerbated by repeated cycles of melting and solidification and later, heating and cooling in AM processes resulting from their layer-by-layer approach. The complex thermal cycles experienced by the parts may induce solid-state transformations and therefore change their microstructure and mechanical properties. Therefore, the effects of processing parameters on the part performance are often multifaceted. Discussion of several of these topics follows and includes defects, residual stress, microsegregation, and microstructure.

3. Effect of laser AM processing parameters on build defects

3.1. Sources of porosity in laser welding and laser additive manufacturing

Undesired porosity is a frequent problem in laser-based AM and manifests itself in two distinct variations. First, lack of fusion defects occurs when insufficient energy is applied to the material, leading to a small melt pool and incomplete melting. Due to the shape of the melt

pool and overlapping patterns, lack of fusion defects tends to be thin and crescent-shaped. On the other hand, when the energy input is high, the metal readily vaporizes and creates gas bubbles that may become trapped due to keyhole instability. In such cases, round pores are observed. The AM community has studied the issue of porosity quite extensively and a general relationship between porosity and the processing parameters of laser power and scan velocity is shown in Fig. 2. The precise parameters at which these conditions occur depends on the material. In general, Fig. 2 suggests that fully dense parts can be achieved with coupled increase of laser power and scanning velocity. However, this generalization neglects a few important nuances which are discussed below.

3.1.1. Keyhole porosity

The key factors contributing to keyhole porosity are laser power, laser scan velocity, the laser beam profile and its interaction with the powder bed. As discussed in Section 2, an increase in energy density causes the melt pool to transition from a conduction mode to a keyhole mode. Thus, the general solution to avoid keyhole porosity is to simply reduce laser power, or to increase the scanning speed. Since keyhole porosity is fully controlled by the melt pool dynamics, it is nearly unaffected by changes in the layer thickness and hatch distances. Scan strategy can also affect the occurrence of keyhole porosity and can be observed in locations where the laser path results in an increased local dwell times, thus increasing the energy density. For example, while executing an L-shaped turn, the laser temporarily slows to change direction, resulting in a reduction of the scan velocity at the elbow of the "L". For this reason, most common scanning strategies are designed so that these turns are not made while the laser is in contact with the material.

King et al. [49] derived an analytical solution for the transition between conduction and keyhole modes as a function of materials properties and AM processing parameters. Above a certain threshold of imparted energy, which is related to the laser power (P) and travel speed velocity (V) as P and $V^{-1/2}$ respectively, the transition from conduction to keyhole mode occurs. This means that the laser power has a greater effect on the development of keyhole porosity than velocity and, at higher power, it becomes increasingly more challenging to eliminate keyhole porosity.

More recent work by Cunningham et al. [50] showed that while the transition between conduction and keyhole mode during laser powder bed fusion techniques is well defined based on energy density, it does not precisely correlate with the shape of the melt pool (Fig. 3). The result is that porosity associated with keyhole vapor instability may be generated before visible "trenching" is observed in the melt pool shape, and the boundary between fully-defense parts and keyhole

porosity, shown in Fig. 2, should be viewed as a large zone of uncertainty instead of a sharp boundary. Thus, to minimize porosity, process parameters far away from the boundary should be considered.

3.1.2. Lack-of-fusion porosity

In contrast with keyhole porosity, lack-of-fusion porosity depends on both the melt pool size as well as the scanning pattern. The boundary for lack-of-fusion is determined by full melting of the material, which is achieved through complete overlap of the melt pool. Thus, with knowledge of the melt pool shape and size, it is possible to analytically determine processing parameters that may lead to conditions where full melting is achieved. A number of different criteria have been proposed to define full melting; from the simple "lack of fusion index" (LF), defined as the ratio between the melt pool depth and the layer thickness, to a more complex analytical calculation that accounts for fluid dynamics in the melt pool [1]. A middle-ground approach uses geometry of the melt pool and simulates a series of overlapping semi-circles or semi-ovals. For a given melt pool size, the minimum depth of overlap is defined as schematically shown in Fig. 4 as M_d^0. This quantity is affected by the hatch distance of the melt pool, which then dictates a maximum layer thickness. During fabrication, a layer thickness smaller than M_d^0 must be selected to ensure that lack of fusion does not occur in between successive deposits. Similarly, due to the natural variations in laser power output, laser-powder absorption, and laser scan speed, the boundary between lack-of-fusion and fully dense parts should be treated as contours of confidence intervals for presence of porosity.

Therefore, while keyhole porosity is primarily a melt-pool level effect that depends mostly on power and velocity, lack of fusion porosity is a composite effect that heavily involves scan strategy. The user can configure the parameters as appropriate based on other needs such as microstructure, properties, or production-related limitations. For example, if a certain power/velocity combination is required to achieve a desired grain morphology, the hatch distance and layer thickness can be adjusted to eliminate lack of fusion. Similarly, if layer thickness is restricted by available size distribution of the powder stock, other parameters can be adjusted accordingly. Finally, we note that the geometry of the actual melt pool can fluctuate quite significantly, so process parameter selection should incorporate sufficient tolerance to minimize porosity.

3.2. Preferential evaporation

Due to the large energy input, the material vaporization temperature is often reached in AM techniques. These evaporative losses are closely related to the maximum temperature reached, and the temperature-dependent vapor pressures of the constitutive elements. When there is a significant difference between the volatility of various elements in the alloy, the overall composition may change after fabrication due to preferential evaporation. For example, this effect has been clearly documented during additive manufacturing of various aluminum-containing alloys such as titanium aluminides [49–54], or Ti-6Al-4V [55]. When processing parameters are not optimized, preferential loss of up to 8 at.% Al have been reported [52].

Alternatively, <0.5% loss in the same alloy can be achieved by controlling the processing parameters. Of critical importance is the linear energy density (laser power to velocity ratio), by minimizing the linear energy density, the preferential loss is reduced [49,51]. However, this must be balanced by the requirement of achieving full melting and elimination of lack-of-fusion defects. For example, agreement has been demonstrated in the study of optimized linear energy density for the $Ti_{48}Al_{48}Nb_2Cr_2$ alloy, where 0.15 J/mm yielded a good combination of a fully-dense material and minimized Al loss [49,51]. Similar correlation between linear energy density and aluminum loss was reported in Ti-6Al-4V, and an optimal value was found to be between 0.1 and 0.2 J/mm. The approach for reaching this value, either through high power and high speed, or low power and low speed did not seem important [53]. Klassen et al. [53], have also reported that when the planar energy
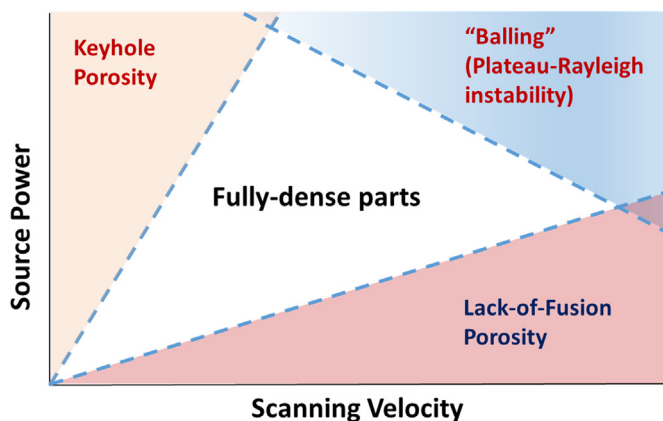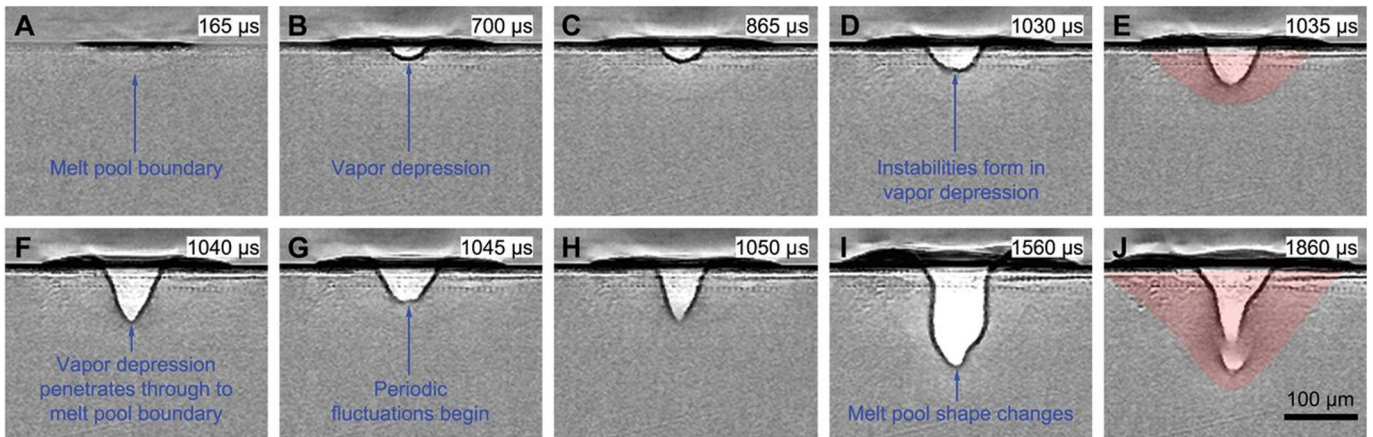
Fig. 2. Illustration of processing parameter influence on porosity: whereas keyhole porosity appears in the high power/low velocity regime, lack-of-fusion porosity appears in the low power/high velocity regions of the processing parameter space.

Fig. 3. Time-lapse synchrotron imaging of a melt pool under static laser [50]: the transition between conduction and keyhole mode begins approximately after 1030 μs after exposure (D–F), but the shape of the melt pool does not change until much later (I–J).

density is kept constant, the linear energy component had a much greater influence on Al loss than hatch distance (Fig. 5). This group of studies suggests that preferential elemental evaporation is a melt pool phenomenon and is most directly related to the maximum temperature reached during fabrication.

In non-aluminum containing alloys, similar preferential evaporation is also observed. Chromium loss occurs in the AM fabrication of Inconel 718 [56], while nickel loss is observed for NiTi alloys [57]. Similarly, it was also found that preferential evaporation of Ni occurs during laser welding of NiTi, thus changing the transformation temperatures of the alloy along the fusion zone [57]. Furthermore, it was found in powder bed fusion fabricated NiTi alloys that the hatch distance may also have a considerable influence on preferential evaporation. When the laser power and speed were kept constant, a change in the hatch distance from 120 to 35 μm was found to increase the Ni loss by 1 at.% in Ni-rich NiTi [58]. Based on this result, it is likely that preferential evaporation may be related to both the maximum temperature reached in the melt pool, as well as the total exposure time near the maximum temperature. Reducing the hatch distance and layer thickness increases exposure time with a linear dependence, and is more controllable and predictable than maximum temperature within the melt pool. Thus, we suggest that the appropriate linear energy density should be selected first and layer thickness/hatch distance adjusted accordingly.

3.3. Residual stress, distortion and geometric precision

Residual stresses and distortion cause a significant challenge during laser additive manufacturing. A similar problem has been well-documented in the laser welding literature. Residual stresses can be classified based on the scale at which they occur in the material as type I, II and III, as these are observed at the macro, micro or sub-micron scales, respectively. In both laser welding and laser additive manufacturing, residual stresses arise due to the large thermal gradients during the process caused by the localized heating of the material [58-60]. This localized heating causes expansion and shrinkage that must be accommodated by the material surrounding the melt pool and the heat affected zone. If the residual stresses are higher than the yield strength of the material, distortion of the part occurs, with potential detrimental effects on the part functionality as well as the ability for the successful completion of the build. When distortion occurs, it is a mechanism for the material to reach an equilibrium between the internal forces that were generated due to the melting and solidification process. It is possible for the amount of distortion to be significant. If this is the case, the part may not meet the tolerance requirements, rendering it unusable. In the worst-case scenario, the developed residual stresses can be high enough to promote cracking within the material. Conversely, residual stresses in laser-based processes may be advantageous. For example, laser induced bending can make use of the large thermal gradients induced by the process to deform the material to the desired shape [59,61]. Additionally, laser shock peening can be used to generate compressive stresses at the material surface and increasing the material's fatigue resistance [62,63].

Despite several works focused on understanding the origin of residual stresses and distortion in laser additive manufacturing and how to control them, at this moment it is impossible to obtain a completely stress-free part without pre-heating of the substrate. Without sufficient control, the magnitude of the residual stresses regularly exceeds the yield stress of the alloy, creating dislocations, distortions and other defects in the material. The greatest challenge posed by residual stresses comes from the heterogeneous distribution of stress, which results in distortion. Currently, common methods to combat residual stresses include pre-heated substrates, or post-fabrication heat treatments for stress relief. An interesting
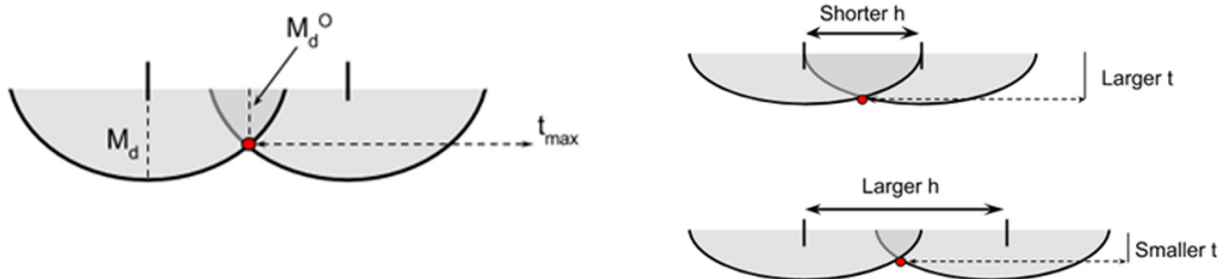

Fig. 4. The criteria for full-melting based on melt pool geometry: hatch distance (h) and layer thickness (t) are coupled parameters given a constant melt pool size. M_d^0 is the minimum layer thickness required to achieve full fusion, and M_d is the melt pool depth.
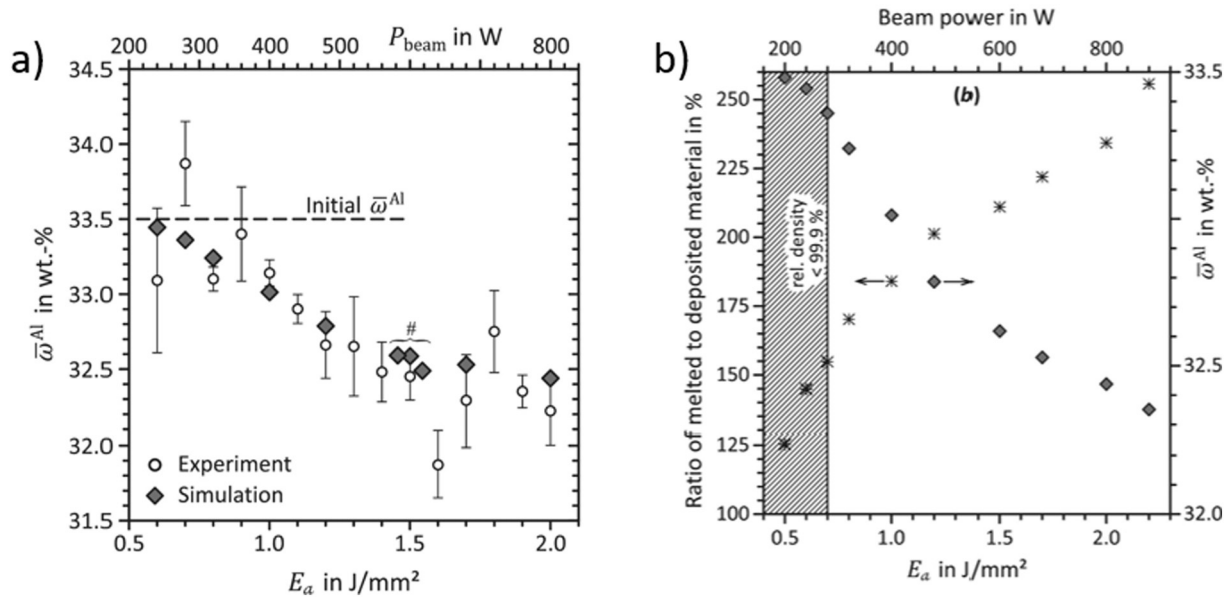
Fig. 5. a) Effect of energy density on aluminum loss during selective electron beam melting of $Ti_{48}Al_{48}Nb_2Cr_2$ alloy, the hatch distance was held constant at 100 μm; b) cross-comparison of relative density and aluminum loss as a function of energy density.
(From [51].)

point has been observed, in that, the magnitude of residual stresses increases with increased length of the scan lines. As a result, implementation of scan strategies where a part is divided into smaller "islands", such that the longest uninterrupted line of travel is reduced, has been found to be effective in reducing residual stress.

One potential solution to control residual stresses developed during laser additive manufacturing can be borrowed from laser welding, with a technique called thermal tensioning [62,64]. In this case, an additional heat source moves ahead, besides, behind, or even in a combination of any of these, of the primary heat source. In laser-based additive manufacturing, this extra heat source can be achieved by adding a second laser source into the system or by splitting the laser beam [65]. In order to successfully implement this approach and to properly select the process parameters (power, travel speed and beam spot size) to be used by each heat sources, modelling is required. The main purpose of the secondary heat source it to pre-heat (if it goes ahead of the main heat source) or to post-heat (if it goes behind the heat source) the material. Additionally, by changing the solidification conditions using this method it may be possible to tune the microstructure of each layer. Of critical importance for the secondary heat source is the controlled and uniform heating of the surrounding material, thus, a low power and defocused beam is likely to be the most effective approach.

Another approach to decrease residual stresses build up and distortion may be the use of sacrificial material, or supports, to serve as mechanical anchors to restrain part deformation [66]. However, the use of support structures subsequently requires the need for removal of these structures, thus increasing production times and material waste. It is best practice to avoid excessive support structures through optimization of the part design, aiming at using minimal support structures to decrease any extra material that will need to be removed. Fig. 6 summarizes how different process parameters during powder bed fusion can be used to overcome build up defects.

4. Effect of laser AM processing parameters on materials and microstructure

4.1. Rapid solidification microstructure

The solidification microstructure in melt-pool based techniques is readily described by temperature gradient (G), solidification growth rate (R), undercooling (ΔT), and materials-related parameters such as composition and liquid diffusivity [67]. Laser welding and laser-based AM techniques share a common space where both large temperature gradient and high growth rates are observed. The high growth rate results in a low-to-moderate G/R ratio and pushes the microstructure towards a planar or cellular structure instead of a dendritic one. Cellular structures are commonly observed in laser welding and laser-based AM techniques [67,68]. The effects of G and R on the developed microstructures are summarized in Fig. 7. It has been found that cellular structures have an impact on the mechanical properties of the part and the size and aspect ratios can be controlled by varying different processing parameters (Fig. 8). Further, for parts made by AM processes, the material experiences a larger number of re-melting passes as compared to a laser welded joint. Depending on the hatch distance used, the microstructure of AM processed samples is dominated by features similar to those found in the heat affected zones (HAZ) of laser welded joints rather than that typical fusion zone microstructures [69,70].

Compared to conventional welding, most of additive manufacturing techniques have high solidification rate (R), and moderate temperature gradients, except for the first processed layers. This means that the cellular dendritic, columnar dendritic, and equiaxed dendritic are the most commonly observed structures. Furthermore, a high solidification rate means that the grain structure is generally very fine, making AM-fabricated samples generally stronger but less ductile than their cast counterparts, provided that process defects, such as porosity and cracking, can be avoided.

While columnar and cellular dendritic structures are commonly observed in welded joints, the layer-by-layer nature of AM process creates a unique mechanism for the dendritic microstructures to change grain morphology through the process, enabling a size shift to features on a larger scale. The size of cellular structures in AM processed or (laser) welded parts are generally on the order of 0.1–1 μm, depending on the parameters used. Under some conditions, cylindrical column-like grains, >10 μm in diameter, and several mm in length are observed, typically for conditions of high power/high scan speed. Additionally, provided that the process parameters are well controlled, it has also been demonstrated to be possible to create single crystal parts by fusion-based AM techniques [71,72].

When columnar grains result in as-built AM parts it is observed that the microstructure is strongly textured (Fig. 9). The grains have preferred

Problem encountered	Primary approach	Secondary approach
Keyhole porosity	Reduce laser power	Increase laser velocity Remelting/reheating
Lack-of-fusion porosity	Reduce scan line spacing Reduce layer thickness	Reduce laser velocity Increase laser power Remelting/reheating
Composition change	Reduce laser power Increase laser velocity	Increase scan line spacing Increase layer thickness
Reduce residual stress and distortion	Reduce scan vector length Use heated substrate/chamber	Reduce laser velocity

Fig. 6. Summary of how process parameters in laser powder bed fusion can be used to combat various build defects.

orientations in the ⟨100⟩ directions perpendicular to the substrate, as similarly observed in the fusion zone of welds, due to ⟨100⟩ being the energetically preferred growth direction for cubic materials [73]. This is related to the fact that this direction is the least close packed, allowing a faster growth compared to other crystallographic directions. It is interesting to note that some materials systems, such as nickel-based alloys, are more prone to formation of grains with differing orientations, or stray grains [71]. The reason for stray grain formation is believed to be related to constitutive supercooling [74], where segregation of the solute atoms ahead of the solidification front modifies the solidification temperature of the alloy to increase the degree of undercooling without physical changes in the temperature or the temperature gradient. Since higher undercooling promotes equiaxed dendritic formation, microsegregation that locally lowers the melting point may increase the likelihood for additional nucleation ahead of the dendritic front and disrupt the columnar growth. This means that during AM processing of alloys, cases where significant microsegregation is expected may require larger temperature gradients (thus higher power), or a velocity-dependent partition coefficient close to unity (higher scan speed). Practically speaking, this means that alloys where stray grain formation is more likely to occur will also tend to solidify in an equiaxed manner without significant texture.

Processing maps have commonly been adapted for individual alloys and used in AM to guide microstructure prediction. Further, G and R can then be translated into relevant processing parameters, such as energy source power and scanning velocity, to create a process map that is easily interpreted. For example, higher scanning velocities result in an increase of R and are conducive to the formation of highly textured columnar grains, while lower scanning velocities favor equiaxed grains with random texture [67]. Conversely, increasing the energy source power tends to increase the temperature gradient, G. It is important to note that the values of G and R are not constant inside the melt pool. Towards the top of the melt pool, R is high while G is low and towards the bottom of the melt pool R is low and G is high. The difference in R and G within the melt pool can differ by an order of magnitude. Predictions of grain morphology must take into consideration the remelting process, where grain features near the bottom of the melt pool are preserved, while grain features near the top of the melt pool are eliminated due to overlap of the melt pool from the adjacent layers.

4.2. Micro-segregation and precipitation of unexpected phases

As a result of the dendritic solidification encountered in laser powder bed fusion there is enhanced formation of unexpected or undesired phases at, or near, segregation zones. In Inconel 718, δ-phase formation has been reported [76] in the as-processed condition of the laser-melted material. This result is surprising as δ-phase is not expected to form at high temperatures in Inconel 718 and, its formation at intermediate temperatures, is usually subject to slow kinetics (on the order of 100 h
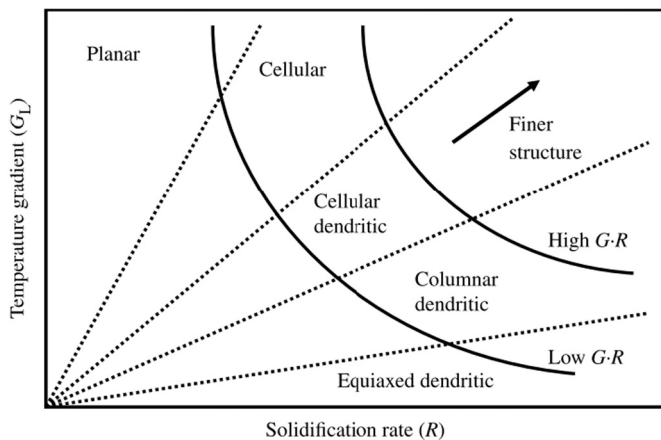

Fig. 7. Effect of temperature gradient (G) and solidification rate (R) on the developed microstructures.
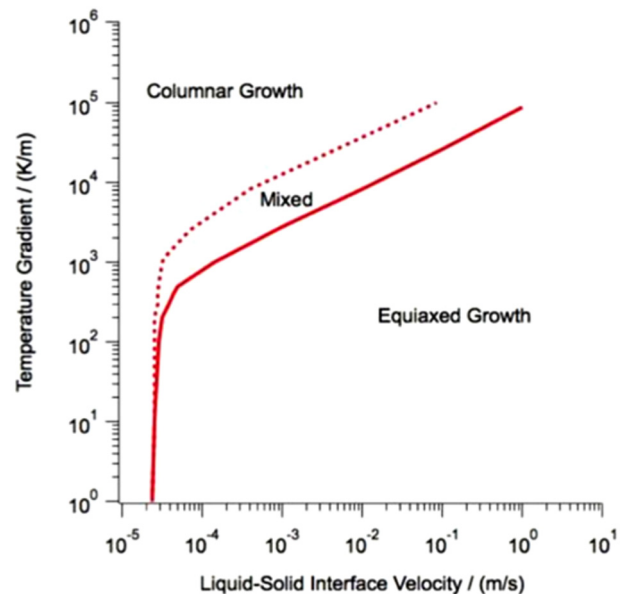(From [67].)

Fig. 8. Solidification map of Inconel 718, highlighting the columnar, equiaxed and mixed solidification microstructures [68].
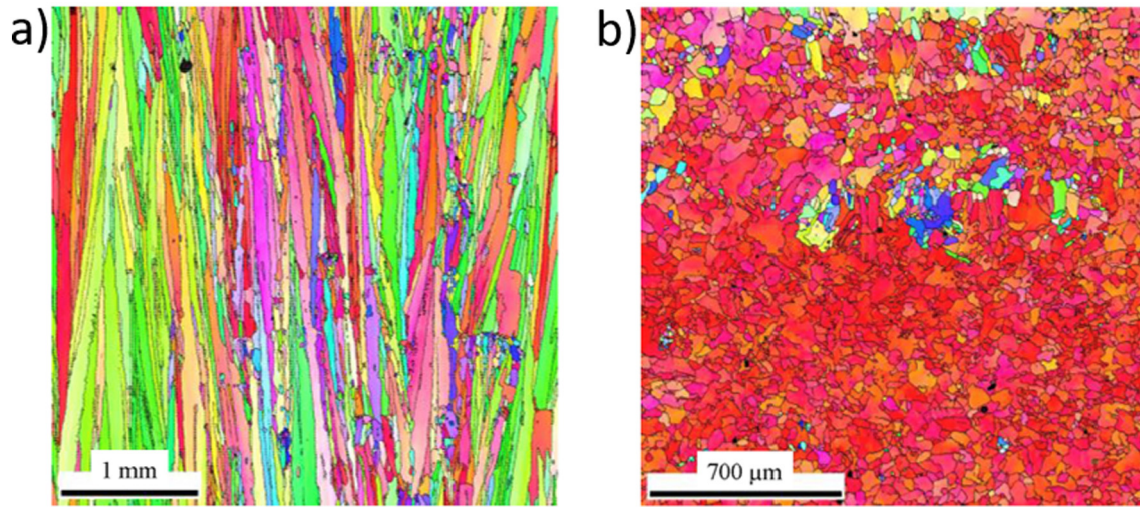
Fig. 9. (a) Side and (b) top views of columnar grains during selective laser melting of IN 718 [75].

at 900 °C) and typically evolves after the γ″ metastable precipitates [77]. As the δ-phase is generally incoherent and adversely affects mechanical properties of the alloy, its presence immediately after AM fabrication is concerning.

Idell et al. [76] reasoned that the unexpected δ formation was attributed to microsegregation during processing, supported by the observation of strong niobium segregation within the interdendritic regions. The typically observed nominal composition of niobium is 3.2–3.6 at.%, while niobium concentration at some interdendritic locations exceeded 8 at.%, allowing δ to become stable at higher temperatures and form directly upon solidification. Furthermore, during conventional heat treatments used to relieve residual stress in Inconel 718 (above 1000 °C for at least 1 h), the δ phase grows and coarsens due to the local changes in chemical composition. Additionally, similar formation of δ phase has been found in Inconel 625 [78]. In this case, although the formation of δ-phase was not observed in the as-built condition, it appeared readily during a stress-relief heat treatment at 800 °C or 870 °C of 1–4 h. The cause of the δ-phase formation is the similar segregation of niobium and molybdenum at the interdendritic regions, as seen in Fig. 10. As a

result, post-processing such as hot isostatic pressing, can negatively impact material performance as crack propagation begins at δ-rich regions at the interdendritic zone [79,80].

High resolution microstructural characterization of additively manufactured steel shows similar relevant issues for consideration. In a Fe-19Ni-xAl maraging steel created by direct laser deposition, Kürnsteiner et al. [81] showed that increasing the aluminum content at the expense of iron and nickel creates an increasing amount and size of NiAl nanoprecipitates in the interdendritic regions where aluminum enrichment occurred (Fig. 11a). At 3.4% Al, the distribution of Al is largely uniform even in the interdendritic space. However, at 8% Al, clustering occurs and precipitate boundaries become clearly visible. Further, at aluminum contents above 15%, a large volume fraction of NiAl precipitates ranging between 2 and 3 nm in size are present as identified through atom probe tomography. Similar reports of nanoprecipitation in the as-processed condition of a 300 series maraging steel has been reported by Tan et al. [82] with the nanoprecipitates coarsening upon subsequent aging. While it is not clear what the structure and composition of the precipitates in the as-processed samples are, the authors identify
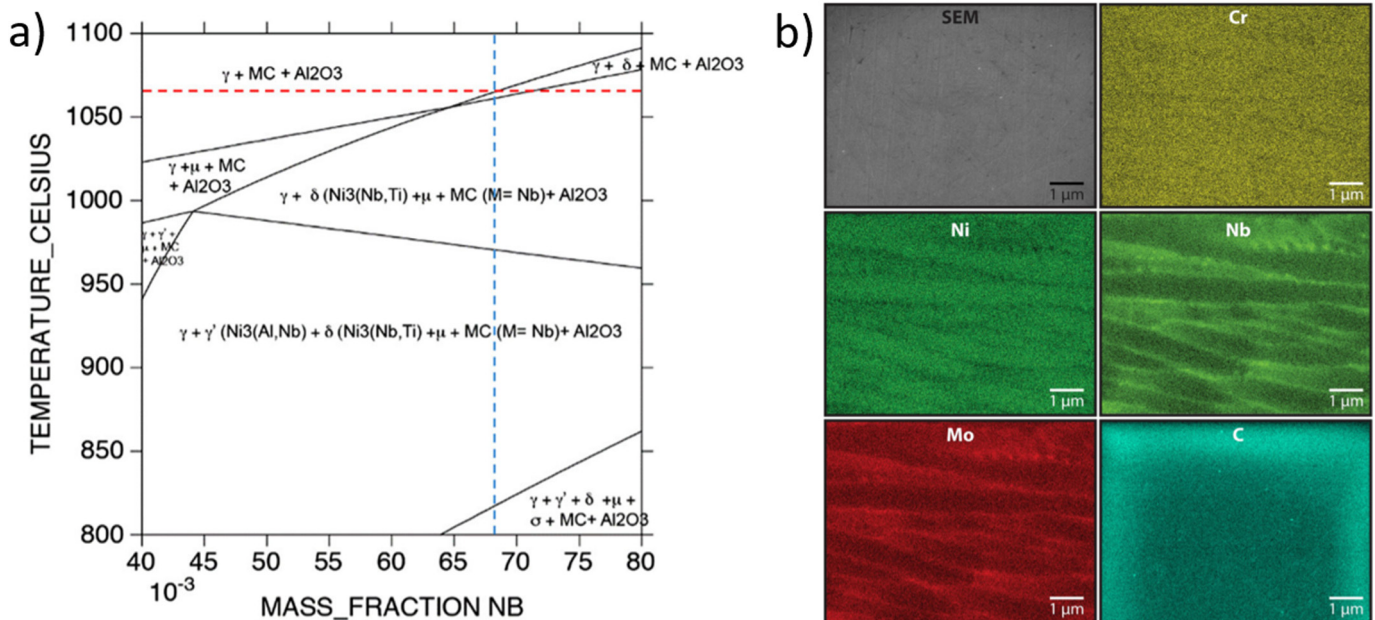

Fig. 10. a) Predicted pseudo-binary phase diagram for Inconel 718 [76] showing the effect of niobium enrichment at interdendritic zones; b) EDS composition mapping showing the clear segregation of niobium and molybdenum in Inconel 625 fabricated through SLM [78].

two types of precipitates in the aged condition: hexagonal η-Ni₃Ti and orthorhombic Ni₃Mo and Ni₃Al.

Finally, it was reported that Ti₂Ni type precipitates were found (Fig. 11b) in selective laser melted Ni-rich NiTi shape memory alloys in the as-processed condition [58,83]. Ti₂Ni is not usually expected to form in Ni-rich compositions unless oxygen or carbide stabilization occurs [84], but its presence was caused by incomplete cellular structures which led to titanium enrichment at the boundaries. These particles are further stabilized by oxygen and thus pose a major problem as they cannot be removed by solution treatments. Regardless of the specific alloy, unexpected phase formation linked to dendritic segregation appears to be a common theme in AM-processed alloys. The phases formed are often detrimental to the properties of the alloy and cannot be easily removed from post-processing. Nevertheless, these phases do not always form in the as-fabricated condition and are highly dependent on the nominal composition. Therefore, designing alloys specifically for AM process and with compositions resistant to microsegregation may be an effective technique to combat this problem.

As previously discussed, microsegregation from dendritic solidification causes unexpected and undesirable phase formation. This is known as solute trapping and strongly depends on the speed of the solidification front and the *equilibrium* partition coefficient, k_e, defined as the ratio between the concentration of an element in two phases, for example, liquid (C_L) and solid (C_S):

$$\frac{C_s}{C_L} = k_e \tag{1}$$

Some of the earliest estimations of microsegregation come from Scheil [85], who described the composition variations ahead of a solidification front with the following assumptions: a) negligible diffusion within the solid; b) complete mixing of solute in the liquid (infinitely fast diffusion), and c) equilibrium near the liquid/solid interface. The resulting equation including these points takes the form:

$$c_s = k_e c_0 (1-f)^{k_e-1} \tag{2}$$

where c_0 is the average composition of the alloy and f is the fraction of the material that is in the solid phase. When experimental techniques made it possible to reliably measure the composition distributions within alloys, it became clear that the Scheil equation was a poor quantitative predictor of the actual solidification process. For most conventional solidification processes, the major issue is the assumption of negligible diffusion in the solid. A model by Brody and Flemings [86] was subsequently introduced to address this weakness. Several variations have since been developed from the Brody-Flemings model and are known as back-diffusion models.

In AM processes, however, the assumption of negligible diffusion in the solid state is less problematic due to the very high cooling rates. Instead, the Scheil model becomes inadequate in other assumptions. Namely, the rapid solidification front (generally 0.01–10 m/s [1]) creates significant undercooling near the dendritic tip because of solute buildup. This means that the liquid composition is no longer homogeneous and changes, depending on the solidification conditions near the solid-liquid interface, may occur. Burden and Hunt [87] have described the undercooling (ΔT) as:

$$\Delta T = \frac{GD_L}{R} + \left[\frac{-8m(1-k_e)c_0\Gamma R}{D_L} \right]^{1/2} \tag{3}$$

where G is the temperature gradient, D_L is the liquid diffusivity, R is the interface or solidification velocity, m is the liquidus slope, and Γ is the Thompson-Gibbs coefficient (γ/ΔS): the ratio between the interfacial energy and the entropy of fusion. This equation provides two important pieces of information. First, the undercooling becomes very large when very high velocities are achieved. This condition is satisfied for most metal AM techniques, particularly those based on powder bed fusion. Second, the effect of temperature gradient on undercooling is highly dependent on the G/R ratio. When G/R is large, the first term on the right side of equation dominates and the gradient has a significant impact on undercooling. When G/R is relatively small, the second term in the equation dominates and the effect of undercooling on temperature gradient is reduced. It has been reported that the temperature gradient during fusion-based AM processes is around 500 K/mm [86,88], and undercooling in powder bed fusion can exceed 50–100 K [1]. Undercooling is one determining factor in solidification grain morphology since it drives dendritic growth and the composition near the dendritic tip. As shown in Fig. 12, undercooling values around 200 K are enough to reach ideal solution conditions in a Ni-Cu-Co alloy [89] where velocity-dependent partition coefficient becomes one. At this state, the alloy will solidify without microsegregation.

It is important to note that microsegregation is not necessarily a detriment to be avoided. Recent studies in 316L stainless steel have shown that additively manufactured parts based on this material have
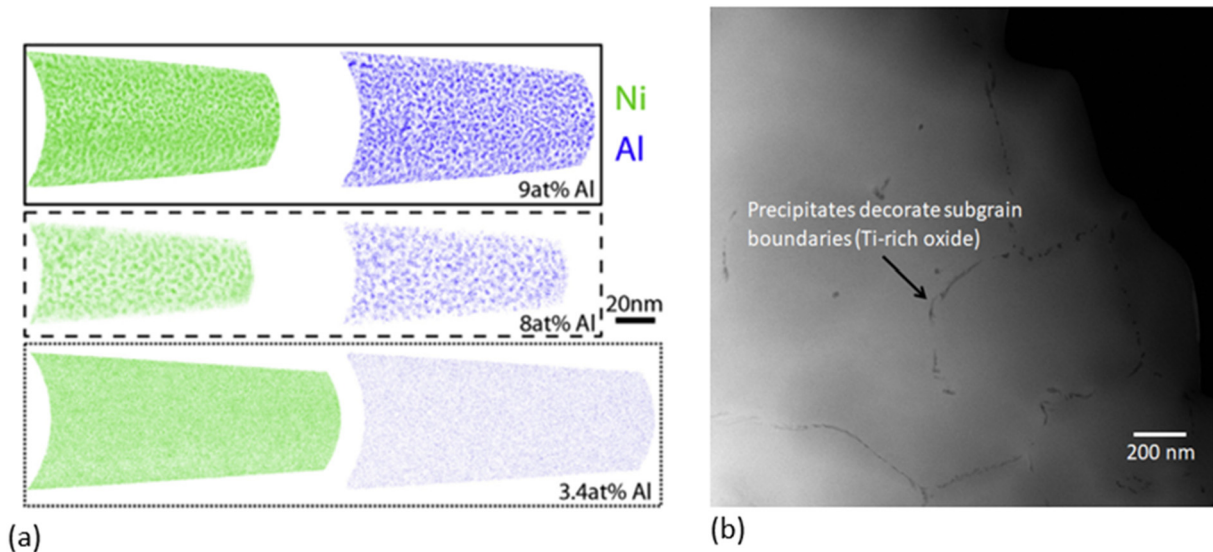

Fig. 11. a) Atom probe tomography mapping of nickel and aluminum composition in as-fabricated (Ni₈₅Fe₁₅)₁₀₀₋ₓAlₓ alloys of various Al content [81]. Clustering and formation of NiAl precipitates becomes visible at Al content above 8 at.%; b) TEM micrograph of SLM Ni-rich NiTi in the as-processed condition [56]. The precipitates are found to be Ti₂Ni at the boundaries.
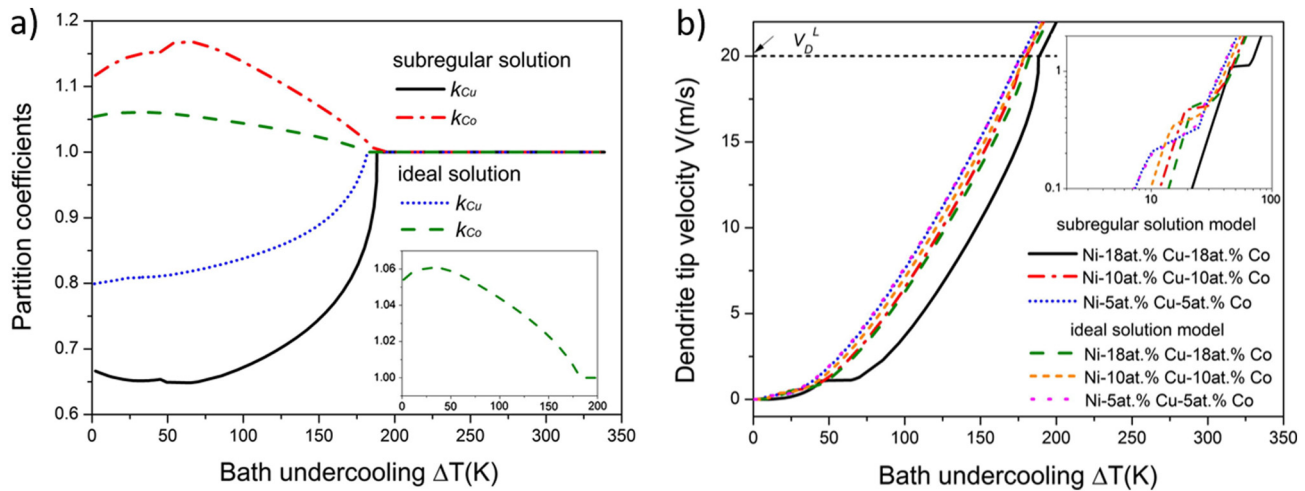
Fig. 12. Effect of undercooling on partition coefficient (a) and solidification velocity (b) for a Ni-Cu-Co alloy: undercooling values of approximately 100 K are reported during solidification in powder bed fusion, which places it in the range where significant changes in velocity-dependent partition coefficient can be expected [89].

simultaneously improved strength and ductility compared to their wrought counterparts (Fig. 13a) [90]. This is a significant development since overcoming the strength-ductility tradeoff is a major goal that drives the development of new metal processing techniques. The origin of the improvement comes from the unique cellular microstructure formed during solidification due to microsegregation. In addition to being enriched with solute elements, the cell wall area is filled with a high density of dislocation networks in contrast to the relatively dislocation-free cell interiors (Fig. 13b). It is believed that this type of layered structure effectively resists both dislocation motion and crack propagation, and can only be created in alloys where significant microsegregation is experienced during processing.

Based on the previous discussion in this section, it is possible to control microsegregation through control of temperature gradient (G), solidification velocity (R), and undercooling (ΔT). The most direct effect would come from the increase in R. At very high R, the non-equilibrium partition coefficient approaches unity and solution trapping is eliminated. In practice, the increase of R is directly related to the velocity of the energy source. Thus, it is desirable to have the maximum scan speed possible while still avoiding lack-of-fusion defects. Increasing the scan speed also requires an increase in laser power, in this case it is important to optimize the power to avoid keyhole porosity in the high-power processing regime. On the other hand, sufficiently low solidification velocity can drive the process into the planar solidification regime (Fig. 7). This has been observed in the lower portions of the melt pool in alloys processed with low laser velocities [91].

Alloy-to-alloy differences are mostly expressed in the quantities of liquid diffusivity and equilibrium partition coefficient. These represent the upper and lower bounds for potential microsegregation. In most alloys, this information can be obtained directly from the phase diagram in the composition difference between the liquidus and solidus at a given temperature. A stronger tendency of microsegregation is found in alloys with large differences, for instance Ni-Al, compared to alloys with smaller differences, for example Ti-6Al-4V. However, it is important to note that microsegregation in real alloys often come from minor alloy elements, such as Nb in Inconel or Cr in 316L stainless steel.

As expressed in Eqs. (2) and (3), an increase in the liquid diffusivity tend to reduce the contribution of solidification velocity. In other words, solute trapping effect is magnified when liquid diffusivity is low and the equilibrium composition cannot be easily reached in the liquid state. On the other hand, the equilibrium partition coefficient acts as the maxima on how much chemical segregation can occur when solute trapping or interfacial stability conditions are not met. Unfortunately, the value of the liquid diffusivity of alloys is difficult to determine, particularly in
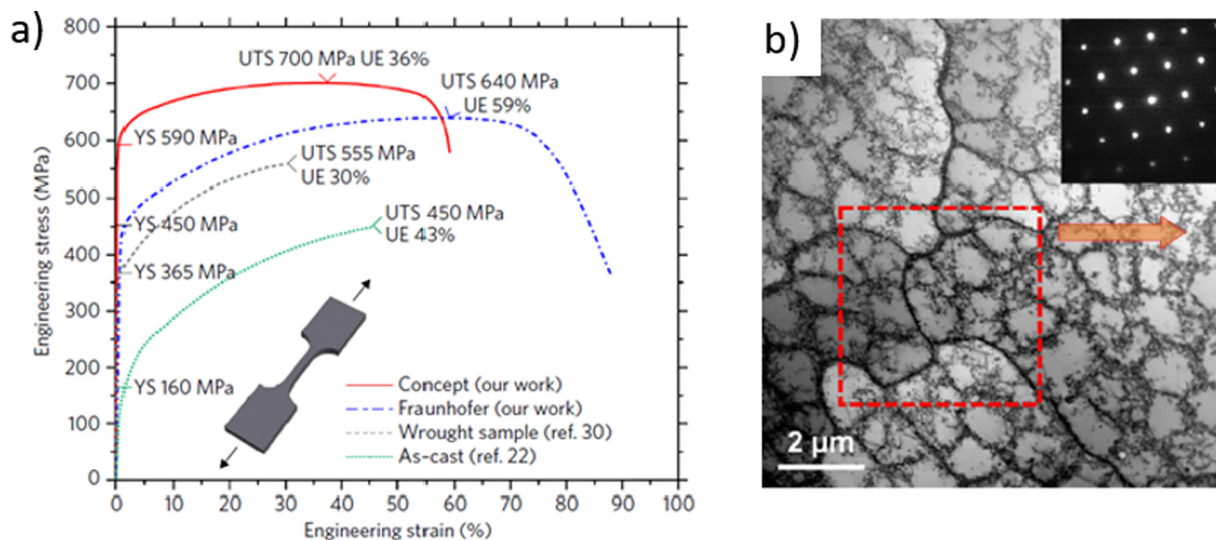

Fig. 13. (a) Comparison between the stress-strain response of wrought and laser powder bed fusion 316L stainless steel, and (b) the unique cellular microstructure observed in the latter [90].

Problem encountered	Primary approach	Secondary approach
Microsegregation	Increase laser velocity	Strongly reduce laser velocity
Undesired texture	Reduce laser velocity	Reduce laser power
Coarse/columnar grains	Reduce laser velocity	Reduce laser power
Meta-stable phases (e.g. martensite)	Remelting/reheating	Reduce laser velocity

Fig. 14. Summary of how process parameters in laser powder bed fusion can be used to combat various microstructure and materials-related issues.

complex engineering alloys commonly used for AM processes, and no single widely accepted model has been developed. Most literature values are based on pulsed ion-beam melting or calculated through ab initio atomistic simulations and typically these values fall in the order of 10^{-9} m^2 s^{-1}.

A summary of how different process parameters during powder bed fusion can be used to overcome microstructure and materials-related problems is presented in Fig. 14. We note that most of the materials-related effects are primarily determined at the melt pool level since microstructure is primarily controlled by solidification characteristics. However, scan strategy can play an indirect, but significant effect especially when sample sizes are small. Generally, parts are printed with a combination of hatch pattern (the inside fill) and contour (the border) and different process parameters are used for each. Barba et al. [92] reported that the α lath thickness reduced significant with sample size in Ti-6Al-4V, while prior β grain structure evolved from one that is coarse and highly texture to a fine, equiaxed and randomly texture case when the sample thickness was reduced to 0.5 mm. This change was explained by the increasing importance of the contour pattern relative to the hatch pattern as sample size was reduced. Of course, the contour pattern parameters could be controlled to yield different microstructures as needed, but such settings should be properly considered when creating parts with small features.

5. Conclusions

Currently, there are multiple process parameters that can be varied during fusion-based additive manufacturing processes. The complex thermal cycles experienced by the material during AM processes often makes it difficult to achieve a single objective without affecting others, and further optimization process is a careful balancing act between competing needs. Nevertheless, the community has good understanding of the effects of the most important process parameters during laser-based additive manufacturing and their impact on porosity formation, preferential evaporation, residual stresses and microstructure. We summarize some of these rules-of-thumb in Fig. 6 (for build defects), and Fig. 14 (for materials and microstructure-related features). Future studies should also explore detailed material and microstructure mechanisms, for example the microsegregation phenomena, dislocation and subgrain boundary structures, controlled formation of desired grain-boundary textures and character, and roles of the melt pool boundary. There remains a significant opportunity to further understand and develop both process parameters and alloys specialized for the part and application of interest. This bespoke nature in both processing and materials selection a unique aspect of additive manufacturing.

Furthermore, the unique control of the AM process allows process parameters to be varied at different physical locations with the same part. For example, porosity at locations designed to bear compressive load in a part is less likely to cause failure compared to porosity at locations design to sustain tensile stress. However, successfully application of location-dependent techniques is predicated upon thorough understanding of the fundamental science of the process and may return a new approach to design where the AM process is considered a component of an integrated system instead of a separate step in a production chain.

CRediT authorship contribution statement

J.P. Oliveira: Conceptualization, Writing- Original Draft, Writing - review and editing. **A.D. LaLonde:** Writing - reviewing and editing. **J. Ma:** Writing- Original Draft, Writing - review and editing.

Declaration of competing interest

The authors declare that they have no known competing financial interests or personal relationships that could have appeared to influence the work reported in this paper.

Acknowledgements

Data availability

The present manuscript is a review paper and does not contain original data. All data presented in the paper have been referenced appropriately.

References

[1] T. DebRoy, H.L.L. Wei, J.S.S. Zuback, T. Mukherjee, J.W.W. Elmer, J.O.O. Milewski, A.M.M. Beese, A. Wilson-Heid, A. De, W. Zhang, Prog. Mater. Sci. 92 (2018) 112–224.
[2] T.A. Rodrigues, V. Duarte, R.M. Miranda, T.G. Santos, J.P. Oliveira, Materials (Basel) 12 (2019) 1121.
[3] W.M. Steen, J. Mazumder, Laser Material Processing, Springer London, London, 2010.
[4] W. Ren, F. Lu, R. Yang, X. Liu, Z. Li, S.R. Elmi Hosseini, Mater. Des. 76 (2015) 207–214.
[5] E.M. Anawa, A.G. Olabi, J. Mater. Process. Technol. 204 (2008) 22–33.
[6] J. Rahman Chukkan, M. Vasudevan, S. Muthukumaran, R. Ravi Kumar, N. Chandrasekhar, J. Mater. Process. Technol. 219 (2015) 48–59.
[7] J.P. Oliveira, Z. Zeng, S. Berveiller, D. Bouscaud, F.M. Braz Fernandes, R.M. Miranda, N. Zhou, Mater. Des. 148 (2018) 145–152.
[8] S.V. Kuryntsev, A.E. Morushkin, A.K. Gilmutdinov, Opt. Lasers Eng. 90 (2017) 101–109.
[9] J. Sun, Q. Yan, W. Gao, J. Huang, J. Mater. 83 (2015) 120–128.
[10] J.P. Oliveira, Z. Zeng, T. Omori, N. Zhou, R.M. Miranda, F.M.B. Fernandes, Mater. Des. 98 (2016) 280–284.

[11] J.P. Oliveira, Z. Zeng, C. Andrei, F.M. Braz Fernandes, R.M. Miranda, A.J. Ramirez, T. Omori, N. Zhou, Mater. Des. 128 (2017) 166–175.

[12] E.H. Amara, R. Fabbro, J. Phys. D. Appl. Phys. 41 (2008), 055503. .

[13] F.H. Kaplan, J. Powell, J. Laser Appl. 23 (2011), 032005. .

[14] X. Li, J. Xie, Y. Zhou, J. Mater. Sci. 40 (2005) 3437–3443.

[15] A. Kidess, S. Kenjeres, B.W. Righolt, C.R. Klejin, Int. J. Therm. Sci. 104 (2016) 412.

[16] S.A. Khairallah, A.T. Anderson, A. Rubenchik, W.E. King, Acta Mater. 108 (2016) 36–45.

[17] J. Zhou, H.-L. Tsai, J. Heat Transf. 129 (2007) 1014.

[18] M. Pastor, P. Zhao, R. Martukanitz, T. Debroy, Weld. J. - Incl. Weld. Res. Suppl. 78 (1999) 207s–216s.

[19] T.Y. Kuo, S.L. Jeng, J. Phys. D. Appl. Phys. 38 (2005) 722–728.

[20] E. Akman, A. Demir, T. Canel, T. Sinmazçelik, J. Mater. Process. Technol. 209 (2009) 3705–3713.

[21] H. Ki, J. Mazumder, P.S. Mohanty, Metall. Mater. Trans. A 33 (2002) 1831–1842.

[22] Y. Hu, X. He, G. Yu, S. Li, C. Zheng, W. Ning, Int. J. Adv. Manuf. Technol. 90 (2017) 3555–3565.

[23] J. Sánchez-Amaya, T. Pasang, M. Amaya-Vazquez, J. Lopez-Castro, C. Churiaque, Y. Tao, F. Botana Pedemonte, Metals (Basel) 7 (2017) 269.

[24] A. Matsunawa, Sci. Technol. Weld. Join. 6 (2001) 351–354.

[25] J. Zhou, H.L. Tsai, Int. J. Heat Mass Transf. 50 (2007) 2217–2235.

[26] S. Katayama, Y. Kobayashi, M. Mizutani, A. Matsunawa, J. Laser Appl. 13 (2001) 187–192.

[27] A. Fritzsche, K. Hilgenberg, F. Teichmann, H. Pries, K. Dilger, M. Rethmeier, J. Mater. Process. Technol. 253 (2018) 51–56.

[28] H. Zhao, T. DebRoy, Weld. J. 80 (2001) 204–210.

[29] A. Haboudou, P. Peyre, A.B. Vannes, G. Peix, Mater. Sci. Eng. A 363 (2003) 40–52.

[30] L. Quintino, A. Costa, R. Miranda, D. Yapp, V. Kumar, C.J. Kong, Mater. Des. 28 (2007) 1231–1237.

[31] S. Catchpole-Smith, N. Aboulkhair, L. Parry, C. Tuck, I.A. Ashcroft, A. Clare, Addit. Manuf. 15 (2017) 113–122.

[32] G. Vastola, G. Zhang, Q.X.X. Pei, Y.-W.W. Zhang, Addit. Manuf. 12 (2016) 231–239.

[33] Z. Wang, E. Denlinger, P. Michaleris, A.D. Stoica, D. Ma, A.M. Beese, Mater. Des. 113 (2017) 169–177.

[34] T.A. Rodrigues, V. Duarte, J.A. Avila, T.G. Santos, R.. Miranda, J. Oliveira, Addit. Manuf. 27 (2019) 440–450.

[35] L.D. Bobbio, B. Bocklund, R. Otis, J.P. Borgonia, R.P. Dillon, A.A. Shapiro, B. McEnerney, Z.-K. Liu, A.M. Beese, J. Alloys Compd. 742 (2018) 1031–1036.

[36] B.E. Carroll, R.A. Otis, J.P. Borgonia, J.O. Suh, R.P. Dillon, A.A. Shapiro, D.C. Hofmann, Z.K. Liu, A.M. Beese, Acta Mater. 108 (2016) 46–54.

[37] W.J. Sames, K.A. Unocic, G.W. Helmreich, M.M. Kirka, F. Medina, R.R. Dehoff, S.S. Babu, Addit. Manuf. 13 (2017) 156–165.

[38] C. Shen, Z. Pan, D. Ding, L. Yuan, N. Nie, Y. Wang, D. Luo, D. Cuiuri, S. Van Duin, H. Li, Addit. Manuf. 23 (2018) 411–421.

[39] B. Vrancken, L. Thijs, J.-P. Kruth, J. Van Humbeeck, J. Alloys Compd. 541 (2012) 177–185.

[40] G. Pyka, A. Burakowski, G. Kerckhofs, M. Moesen, S. Van Bael, J. Schrooten, M. Wevers, Adv. Eng. Mater. 14 (2012) 363–370.

[41] F. Wang, S. Williams, M. Rush, Int. J. Adv. Manuf. Technol. 57 (2011) 597–603.

[42] E. Chauvet, P. Kontis, E.A. Jägle, B. Gault, D. Raabe, C. Tassin, J.J. Blandin, R. Dendievel, B. Vayre, S. Abed, G. Martin, Acta Mater. 142 (2018) 82–94.

[43] Z. Wang, A.D. Stoica, D. Ma, A.M. Beese, Mater. Sci. Eng. A 714 (2018) 75–83.

[44] L.M. Sochalski-Kolbus, E.A. Payzant, P.A. Cornwell, T.R. Watkins, S.S. Babu, R.R. Dehoff, M. Lorenz, O. Ovchinnikova, C. Duty, Metall. Mater. Trans. A Phys. Metall. Mater. Sci. 46 (2015) 1419–1432.

[45] Y. Chen, K. Zhang, J. Huang, S.R.E. Hosseini, Z. Li, Mater. Des. 90 (2016) 586–594.

[46] Z. Wang, T.A. Palmer, A.M. Beese, Acta Mater. 110 (2016) 226–235.

[47] M. Islam, T. Purtonen, H. Piili, A. Salminen, O. Nyrhilä, Phys. Procedia 41 (2013) 835–842.

[48] D. Dai, D. Gu, Appl. Surf. Sci. 355 (2015) 310–319.

[49] W.E. King, H.D. Barth, V.M. Castillo, G.F. Gallegos, J.W. Gibbs, D.E. Hahn, C. Kamath, A.M. Rubenchik, J. Mater. Process. Technol. 214 (2014) 2915–2925.

[50] R. Cunningham, C. Zhao, N. Parab, C. Kantzos, J. Pauza, K. Fezzaa, T. Sun, A. Rollett, Science 363 (2019) 849.

[51] J. Schwerdtfeger, C. Körner, Intermetallics 49 (2014) 29–35.

[52] L.E. Murr, S.M. Gaytan, F. Medina, H. Lopez, E. Martinez, B.I. Machado, D.H. Hernandez, L. Martinez, M.I. Lopez, R.B. Wicker, J. Bracke, Philos. Trans. A. Math. Phys. Eng. Sci. 368 (2010) 1999–2032.

[53] A. Klassen, V.E. Forster, V. Juechter, C. Körner, J. Mater. Process. Technol. 247 (2017) 280–288.

[54] D. Cormier, O. Harrysson, T. Mahale, H. West, Res. Lett. Mater. Sci. 2007 (2007) 1–4.

[55] V. Juechter, T. Scharowsky, R.F. Singer, C. Körner, Acta Mater. 76 (2014) 252–258.

[56] P. Nandwana, W.H. Peter, R.R. Dehoff, L.E. Lowe, M.M. Kirka, F. Medina, S.S. Babu, Metall. Mater. Trans. B Process Metall. Mater. Process. Sci. 47 (2016) 754–762.

[57] J. Ma, B. Franco, G. Tapia, K. Karayagiz, L. Johnson, J. Liu, R. Arroyai, I. Karaman, A. Elwany, Sci. Rep. 7 (2017), 46707. .

[58] T. Bormann, B. Müller, M. Schinhammer, A. Kessler, P. Thalmann, M. de Wild, Mater. Charact. 94 (2014) 189–202.

[59] J.P. Oliveira, A.J. Cavaleiro, N. Schell, A. Stark, R.M. Miranda, J.L. Ocana, F.M. Braz Fernandes, Scr. Mater. 152 (2018) 122–126.

[60] P.J. Withers, H.K.D.H. Bhadeshia, Mater. Sci. Technol. 17 (2001) 366–375.

[61] P. Mercelis, J.-P. Kruth, Rapid Prototyp. J. 12 (2006) 254–265.

[62] C. Ye, S. Suslov, X. Fei, G.J. Cheng, Acta Mater. 59 (2011) 7219–7227.

[63] R. Sun, L. Li, Y. Zhu, W. Guo, P. Peng, B. Cong, J. Sun, Z. Che, B. Li, C. Guo, L. Liu, J. Alloys Compd. 747 (2018) 255–265.

[64] M.V. Deo, P. Michaleris, Sci. Technol. Weld. Join. 8 (2003) 49–54.

[65] P. Aggarangsi, J.L. Beuth, Proc. SFF Symp., Austin, 2006 709–720.

[66] G. Strano, L. Hao, R.M. Everson, K.E. Evans, Int. J. Adv. Manuf. Technol. 66 (2013) 1247–1254.

[67] S. Kou, Welding Metallurgy, 2nd ed. John Wiley & Sons, Hoboken, NJ, 2003.

[68] H.L. Wei, T. Mukherjee, T. DebRoy, TMS, Proceedings of the 6th International Conference on Recrystallization and Grain Growth, 2016 265.

[69] J.P. Oliveira, R.M. Miranda, F.M. Braz Fernandes, Prog. Mater. Sci. 88 (2017) 412–466.

[70] A. Zinoviev, O. Zinovieva, V. Ploshikhin, V. Romanova, R. Balokhonov, Mater. Des. 106 (2016) 321–329.

[71] A. Basak, R. Acharya, S. Das, Metall. Mater. Trans A 47 (2016) 3845–3859.

[72] S. Chandra, X. Tan, C. Wang, Proc. of the 3rd Intl. Conf. on Progress in Additive Manufacturing, 2018 427–432.

[73] H.L. Wei, J.W. Elmer, T. DebRoy, Acta Mater. 115 (2016) 123–131.

[74] L. Wang, N. Wang, Acta Mater. 104 (2016) 250–258.

[75] E. Cakmak, M.M. Kirka, T.R. Watkins, R.C. Cooper, K. An, H. Choo, W. Wu, R.R. Dehoff, S.S. Babu, Acta Mater. 108 (2016) 161–175.

[76] Y. Idell, L.E. Levine, A.J. Allen, F. Zhang, C.E. Campbell, G.B. Olson, J. Gong, D.R. Snyder, H.Z. Deutchman, JOM 68 (2016) 950–959.

[77] E. Andrieu, N. Wang, R. Molins, A. Pineau, Superalloys 718, 625, 706 Var. Deriv., TMS, 1994 695–710.

[78] E.A. Lass, M.R. Stoudt, M.E. Williams, M.B. Katz, L.E. Levine, T.Q. Phan, T.H. Gnaeupel-Herold, D.S. Ng, Metall. Mater. Trans. A 48 (2017) 5547–5558.

[79] Y. Kuo, K. Kakehi, Mater. Trans. 58 (2017) 1042–1048.

[80] A. Mostafa, I. Picazo Rubio, V. Brailovski, M. Jahazi, M. Medraj, Metals (Basel) 7 (2017) 196.

[81] P. Kürnsteiner, M.B. Wilms, A. Weisheit, P. Barriobero-Vila, E.A. Jägle, D. Raabe, Acta Mater. 129 (2017) 52–60.

[82] C. Tan, K. Zhou, W. Ma, P. Zhang, M. Liu, T. Kuang, Mater. Des. 134 (2017) 23–34.

[83] B.E. Franco, J. Ma, B. Loveall, G.A. Tapia, K. Karayagiz, J. Liu, A. Elwany, R. Arroyave, I. Karaman, Sci. Rep. 7 (2017) 3604.

[84] J.P. Oliveira, D. Barbosa, F.M.B. Fernandes, R.M. Miranda, Smart Mater. Struct. 25 (2016) 03LT01.

[85] E. Scheil, Z. Metallk. 34 (1942) 70.

[86] H.D. Brody, M.C. Flemings, Trans. TMS-AIME 236 (1966) 615.

[87] M.H. Burden, J.D. Hunt, J. Crystal Growth 22 (1974) 109.

[88] V. Manvatkar, A. De, T. DebRoy, Mater. Sci. Technol. 31 (2015) 924–930.

[89] K. Wang, H. Wang, F. Liu, H. Zhai, Acta Mater. 61 (2013) 4254–4265.

[90] Y.M. Wang, T. Voisin, J.T. McKeown, J.C. Ye, N.P. Calta, Z. Li, Z. Zeng, Y. Zhang, W. Chen, T.T. Roehling, R.T. Ott, M.K. Santala, P.J. Depond, M.J. Matthews, A.V. Hamza, T. Zhu, Nat. Mater. 17 (2018) 63.

[91] L. Johnson, M. Mahmoudi, B. Zhang, R. Seede, X. Huang, J.T. Maier, H.J. Maier, I. Karaman, A. Elwany, R. Arroyave, Acta Mater. 176 (2019) 199–210.

[92] D. Barba, C. Alabort, Y.T. Yang, M.L. Vascasillas, R.C. Reed, E. Alabort, Mater. & Design. 186 (2020) 108235.